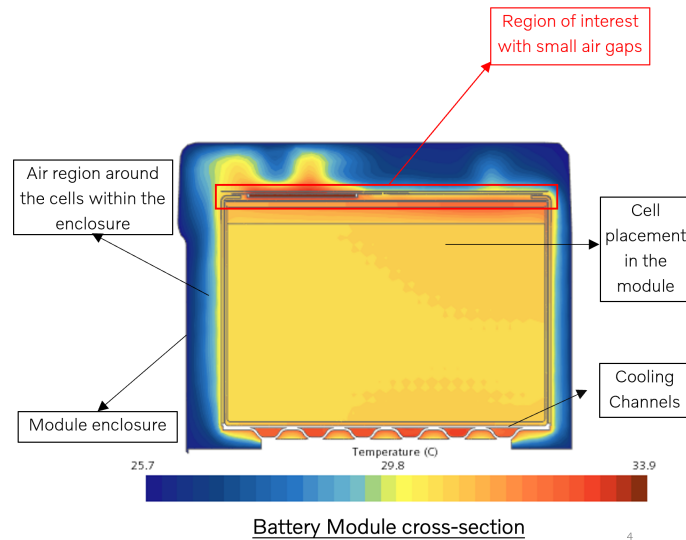
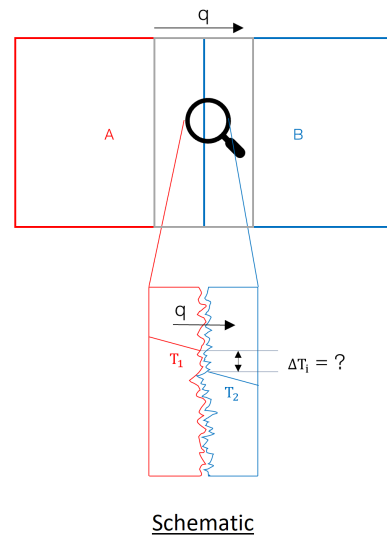




### Macro scale modeling



### Micro scale modeling



# Multiscale battery thermal modeling

## Macro and micro scale model improvements

Master's thesis in Mechanics and Maritime Sciences

AMITH BASAVAPATNA SHESH

DEPARTMENT OF MECHANICS AND MARITIME SCIENCES

CHALMERS UNIVERSITY OF TECHNOLOGY  
Gothenburg, Sweden 2022  
www.chalmers.se



MASTER'S THESIS IN APPLIED MECHANICS

# Multiscale Battery Thermal Modeling

Macro and Micro-scale Battery Thermal Model Improvements

Amith Basavapatna Shesh



**CHALMERS**  
UNIVERSITY OF TECHNOLOGY

Department of Mechanics and Maritime Sciences  
*Division of Vehicle Engineering and Autonomous Systems*  
CHALMERS UNIVERSITY OF TECHNOLOGY  
Gothenburg, Sweden 2022

Multiscale battery thermal modeling  
Micro and macro-scale modeling of a battery module  
Amith Basavapatna Shesh

© Amith Basavapatna Shesh, 2022.

Supervisor: Justinas Peciura, Volvo cars  
Examiner: Simone Sebben, Mechanics and Maritime Sciences

Master's Thesis 2022:35  
Department of Applied Mechanics  
Division of Mechanics and maritime sciences  
Chalmers University of Technology  
SE-412 96 Gothenburg  
Telephone +46 31 772 1000

Multiscale battery thermal modeling  
Micro and macro-scale modeling of a battery module  
Amith Basavapatna Shesh  
Department of Mechanics and maritime sciences  
Chalmers University of Technology

## Abstract

This thesis work concentrates on improving the existing battery thermal model used by Volvo cars. Improvements are brought about in two specific aspects of the battery thermal model; motivation behind choosing these two aspects was to better match the simulation results to the previously conducted test results. The first aspect concentrates on explicitly modeling total heat transfer i.e. conduction, convection and radiation through small air gaps inside the battery module (order of a few mm). Computational Fluid Dynamics (CFD) simulations were carried out using Star-CCM+. Result showed that at a small expense in computational time, a large improvement in accuracy could be attained.

The second part of the thesis concentrates on studying heat transfer across micro asperities. It is of common practice to assume that two seemingly flat surfaces in contact with each other to have perfect conductive heat transfer at the interface. In reality, there are micro asperities as a result of surface roughness, these micro asperities give rise to a thermal resistance at the interface between the two surfaces. Results from this study prove that under certain conditions and for certain material interfaces within the battery module, it would be an oversimplification to make the initial observation about perfect conduction between the two surfaces. A methodology to predict contact resistance in the battery module is successfully established. Further, a sensitivity study was carried out to better understand which material pair(s) inside the battery module contributes the most in terms of thermal contact resistance ( $R_c$ ).

Keywords: contact, resistance, heat-transfer, CFD, thermodynamics, battery



# Contents

<b>Notation</b>	<b>VI</b>
List of Figures . . . . .	VI
List of Tables . . . . .	VI
<b>1 Introduction</b>	<b>1</b>
1.1 Background . . . . .	1
1.2 Objective . . . . .	2
<b>2 Theory</b>	<b>3</b>
2.1 Thermal Heat Transfer . . . . .	3
2.1.1 Conduction . . . . .	3
2.1.2 Convection . . . . .	3
2.1.2.1 Boussinesq Approximation . . . . .	4
2.1.2.2 Incompressible Ideal Gas . . . . .	4
2.1.2.3 Compressible Ideal Gas . . . . .	5
2.1.3 Radiation . . . . .	5
2.2 Thermal Contact Resistance . . . . .	5
2.2.1 Factors Influencing Thermal Contact Resistance . . . . .	7
2.2.1.1 Thermal Conductivity . . . . .	7
2.2.1.2 Contact Pressure . . . . .	7
2.2.1.3 Surface Roughness ( $R_a$ ) . . . . .	7
2.2.1.4 Asperity Slope (m) . . . . .	8
2.2.1.5 Micro-Hardness and Modulus of Elasticity . . . . .	8
2.3 Thermal Contact Resistance Prediction . . . . .	9
2.3.1 Plastic Deformation Models . . . . .	9
2.3.1.1 Cooper, Mikic and Yovanovich Model . . . . .	9
2.3.1.2 Mikic Model . . . . .	10
2.3.2 Elastic Deformation Models . . . . .	10
2.3.2.1 Greenwood and Williamson Model . . . . .	10
2.3.2.2 Mikic Model . . . . .	11
<b>3 Methods</b>	<b>13</b>
3.1 Small Air-gap Modeling . . . . .	14
3.1.1 Mesh Sensitivity . . . . .	15
3.2 Contact Resistance Modeling . . . . .	17
3.2.1 Corner case 1: Maximum heat transfer . . . . .	18

<b>4</b>	<b>Results</b>	<b>21</b>
4.1	Small air gap model improvement . . . . .	21
4.1.1	Summary . . . . .	25
4.2	Contact resistance modeling . . . . .	26
4.2.1	Cell 1 . . . . .	26
4.2.2	Cell 2 . . . . .	29
<b>5</b>	<b>Conclusion</b>	<b>31</b>
5.1	Small air gap modeling . . . . .	31
5.2	Contact resistance modeling . . . . .	31
5.3	Future work . . . . .	31
	<b>Bibliography</b>	<b>33</b>
<b>A</b>	<b>Extra Figures</b>	<b>I</b>

# Preface

In this study, efforts have been made to improve the existing thermal computer aided engineering (CAE) model used by Volvo cars for their battery, to be specific their battery thermal model. Tests previously conducted by the company have been used as a benchmark for the simulation study and since a deviation was observed, improvements have been brought about in this study to reduce the observed deviation.

This project has been carried out with Justinas Pecuire as the industrial supervisor from Volvo cars and Professor Simone Sebben as the examiner. All the work in this project has been carried out at the premises of Volvo cars. I would like to thank all the people that helped me complete this ardent task in the time allotted for the same. I would first like to thank my supervisor, Justinas Peciura at Volvo cars for supporting me throughout the project. His ideas and feed-backs were invaluable and his constructive criticism was inestimable. Further, I would like to thank Nandee Mysore who helped at crucial moments of the project. I would like to extend my gratitude to Marie-Louise Holmer at Volvo for the constant encouragement, opportunity and for the resources extended to me for this project. Finally, I would like to convey my special thanks to Simone Sebben at Chalmers for guiding me and steering me in the right direction.

Göteborg July 2022

AMITH BASAVAPATNA SHESH



# Notations

Below all the notations used in this report is listed.

## Greek letters

$\rho$	Density
$\epsilon$	Emissivity of the surface
$\sigma$	Stefan Boltzmann constant
$\phi$	Greenwood and Williamson plasticity index
$\beta$	radius of micro-asperity
$\gamma$	Mikic plasticity index
$\sigma_s$	Effective surface roughness

## Roman upper case letters

$\Delta T$	Temperature difference between two points in space
$T_S$	Surface temperature
$T_\infty$	Ambient temperature
$P_{abs}$	Absolute pressure
$R$	gas constant
$R_c$	Thermal contact resistance
$R_a$	Surface roughness
$H$	Micro-hardness
$E$	Elastic modulus
$P$	Pressure
$A$	Area
$F$	Force

## Roman lower case letters

$x$	position
$T$	Temperature
$q_{conduction}$	Rate of conduction heat transfer
$q_{convection}$	Rate of convective heat transfer
$k$	Thermal conductivity
$h$	convective heat transfer coefficient
$h_c$	Thermal contact conductance
$q_{radiation}$	Rate of radiative heat transfer
$m$	Asperity slope
$\nu$	Poisson ratio
$k_s$	effective thermal conductivity
$m_s$	Effective asperity slope
$r$	Thermal resistance
$c$	Thermal conductance
$t$	Thickness of the material

# List of Figures

2.1	<i>Heat transfer illustration at micro scale . . . . .</i>	6
2.2	<i>Effect of increased pressure on micro asperities at the interface . . . . .</i>	7
2.3	<i>Effect of decreased surface roughness on micro asperities at the interface . . . . .</i>	8
2.4	<i>Effect of decreased material hardness on micro asperities at the interface . . . . .</i>	9
3.1	<i>Battery module schematic (not to scale) . . . . .</i>	13
3.2	<i>Labelled cross section of the battery module . . . . .</i>	16
3.3	<i>Sensor positions . . . . .</i>	17
3.4	<i>Comparison of small air gap . . . . .</i>	17
3.5	<i>Zoomed in comparison of small air gap . . . . .</i>	18
3.6	<i>Sensor and interface placement for gathered temp. data from test . . . . .</i>	19
4.1	<i>Schematic of mesh deletion and application of boundary heat flux . . . . .</i>	25
4.2	<i>Simulation comparison . . . . .</i>	26
4.3	<i>Test sensor placement for cell 1 . . . . .</i>	27
4.4	<i>Deviation between test and simulation data plotted for different simulations on sensor "Tcel1_F1_C5R5_C1" . . . . .</i>	28
4.5	<i>Deviation between current simulation and baseline simulation on sensor "Tcel1_F1_C5R5_C1" . . . . .</i>	28
4.6	<i>Test sensor placement for cell 2 . . . . .</i>	29
4.7	<i>Temperature deviation between test and simulation data plotted for different simulations on sensor "Tcel2_F3_C5R5_C1" . . . . .</i>	30
4.8	<i>Temperature deviation between current simulation and baseline simulation on sensor "Tcel2_F3_C5R5_C1" . . . . .</i>	30
A.1	<i>Temperature deviation between test and simulation on cell <math>(x - 1)</math> . . . . .</i>	I
A.2	<i>Temperature deviation between current simulation and baseline simulation on cell <math>(x - 1)</math> . . . . .</i>	II
A.3	<i>Temperature deviation between test and simulation data on cell <math>x</math> . . . . .</i>	II
A.4	<i>Temperature deviation between current simulation and baseline simulation on cell <math>x</math> . . . . .</i>	III
A.5	<i>Coarse mesh on cross section of battery module . . . . .</i>	III
A.6	<i>Fine mesh on cross section of battery module . . . . .</i>	IV
A.7	<i>Finer mesh on cross section of battery module . . . . .</i>	IV



# List of Tables

3.1	<i>Labels for Figure 3.1</i>	14
3.2	<i>Deviation observed between test data provided and baseline simulation</i>	14
3.3	<i>Physics models and sub-models used in the improved model</i>	15
3.4	<i>Alternate Physics Models Tested</i>	16
3.5	<i>Mesh independence study</i>	16
3.6	<i>Interface list</i>	19
3.7	<i>Mikic Plasticity Index for corner cases (<math>\gamma</math>)</i>	19
4.1	<i>Simulation bibliography</i>	21
4.2	<i>Simulation description</i>	21
4.3	<i>Contact resistance and interface relation</i>	27
4.4	<i>Interface and simulation list</i>	29



# 1

## Introduction

### 1.1 Background

The automotive industry has seen a phenomenal shift in the past decade towards electric mobility, understandably so given the climate situation in the world especially in terms of greenhouse gas (GHG) emissions and the industry's earlier dependence on fossil fuels, In EU-27 the transportation sector accounted for approximately a quarter of GHG emissions in 2014, of which road transportation accounted for more than 70% (European Commission, 2018). The vast majority (95%) of the transportation energy stems from petroleum-based fuels, such as gasoline and diesel, and more than half of the transportation-related GHG emissions derive from passenger cars and light-duty trucks, according to the United States Environmental Protection Agency (USEPA) (2017) [1]. Hence, the efforts being put into the electrification of automobiles seems justified.

Aiding to the Paris agreement, Volvo cars has decided to go fully electric by 2030. In most modern cars space is limited and the environment in which these cars must be designed to operate in vary quite a bit. With the climate situation in the world and the competition in the market segment, requirements for better performance and efficiency are becoming increasingly relevant, pushing the automotive manufacturers into designing smarter and more advanced vehicles, this means that more components and systems will have to be integrated into the vehicle. Thus, resulting in a higher density of components, which would in-turn require efficient heat management.

Understanding and modeling heat flowing through surfaces in contact is a vital step in thermal network design of batteries. The surfaces in contact have a surface roughness in reality which are seldom taken into account while modeling the heat transfer of modern-day engineering devices.

Traditionally for most applications it is common to consider the surfaces participating in the heat transfer to be flat, neglecting the surface roughness at the microscopic scale. Solid surfaces in contact have surface irregularities both at the microscopic and macroscopic scale, while surface roughness is the term used to measure the surface irregularities arising from the microscopic scale, waviness, surface out-of-flatness and out-of-roundness give rise to surface irregularities at the macroscopic scales. Thus, when two solid surfaces come in contact, even at high contact pressures of the order of 10 MPa they are only in contact at discrete spots. It has been noted that for most

metals, the actual area of contact is only about 1-2% of the nominal contact area [2].

The battery system of modern-day vehicles consists of components made out of different materials with different thermal conductivities. Modeling the heat transfer across the interface between two components plays a vital role in predicting the temperatures on the surface.

Modeling the interface is tricky with a large emphasis on experimental studies, the challenge particularly lies in estimating the macroscopic temperature variation due to the imperfect matching at the microscopic scale. This phenomenon where there is an additional resistance at the interface due to microscopic effects such as surface roughness matching imperfectly is termed as contact resistance.

This master thesis has been carried out in co-operation with Volvo Corporation in the battery CAE department.

## 1.2 Objective

This Master thesis has multiple smaller objectives, these objectives have been set with the aim to improve the overall thermal model to better match the physical test results. While the main objective of this Master thesis is first to develop a method to estimate the **thermal contact resistance** ( $R_c$ ) between different components in an individual battery module and then to check it's sensitivity and significance to the overall temperature prediction, efforts have been made to improve the thermal model currently being used by Volvo Cars; specifically the modeling of small air gaps inside the battery model.

The methodology is developed by combining material tests on individual components to measure parameters required for  $R_c$  modeling, feeding these values into a mathematical model to predict the thermal contact resistance ( $R_c$ ) and finally plugging in these values into the 3D computational fluid dynamics (CFD) simulation in STAR-CCM+.

Efforts to validate the mathematical model have been carried out by physically conducting experiments to calculate  $R_c$ . 3D CFD simulation results have been validated with existing test data provided by Volvo Cars.

# 2

## Theory

This section will cover the findings from the literature survey carried out to fulfill the objective mentioned in the earlier section. Starting with the introduction of the basic theory behind heat transfer, different modes of heat transfer and insights into different models used during the course of the thesis is discussed. the section then evolves to explain  $R_c$ , the different factors that influence  $R_c$  and finally the mathematical model to predict the value of  $R_c$ .

### 2.1 Thermal Heat Transfer

Thermal transfer or heat transfer can be explained as the phenomena where energy transfer occurs between two bodies that have some temperature difference present between them. Following from the second law of thermodynamics, heat transfer always occurs in one fixed direction, from the hotter body to the colder body. Heat transfer has long been categorised into conduction, convection and radiation based on the mode of heat transfer. The effect of each mode of heat transfer in a battery system has been studied and documented in this report.

#### 2.1.1 Conduction

When heat transfer occurs from a region of higher temperature to a region of lower temperature within the same part or between two parts that are physically in contact can be termed as conduction. From *Fourier's Law* it is understood that the rate of heat transfer between two points is proportional to the temperature gradient between the two points.

$$q_{\text{conduction}} = -k \frac{\Delta T_c}{\Delta x} \quad (2.1)$$

Where  $q_{\text{conduction}}$  is the rate of conduction heat transfer per unit area,  $\frac{\Delta T_c}{\Delta x}$  is the gradient of temperature and  $k$  is the thermal conductivity of the material.

#### 2.1.2 Convection

Convection, like conduction requires a medium present between the two regions for heat transfer, however, unlike conduction, convection occurs between two regions that are not physically in contact with each other. In this case heat is transferred by the participating fluid medium present between them due to the molecules of fluid carrying energy from the hotter region to the colder region. there are two

main types of convection, *natural convection* and *forced convection* depending on the velocity of the fluid that interacts between the regions.

In this report, only natural convection is of relevance. Natural convection occurs when a heat source is placed in an enclosed volume which is not vacuum, although there might be no movement of the fluid before the heat source is placed inside the enclosed volume, once the heat source is placed in the enclosed volume, the temperature gradient that gets established in the volumetric space heats up the air, causing it to change its density and expand, thus displacing the molecules of air due to the effect of buoyancy. This induced motion participates in heat transfer and is thus important to be accounted for during the modeling process. From *Newton's law of cooling*, we have the relation between the rate of convective heat loss and difference in temperature between the surface and the temperature of the ambience to which it is losing heat.

$$q_{\text{convection}} = hA(T_S - T_\infty) \quad (2.2)$$

Where  $q_{\text{convection}}$  is the rate of convective heat transfer,  $h$  is the convective heat transfer coefficient,  $A$  is the area of the surface exposed to heat transfer by convection,  $T_S$  is the temperature of the surface and  $T_\infty$  is the ambient temperature. There are three popular approaches available in Star-CCM+ to model natural convection. Star-CCM+ is a commercial Computational Fluid Dynamics (CFD) tool. Within Star-CCM+ the three options available are *Boussinesq approximation*, *incompressible ideal gas*, *compressible ideal gas* [Star-CCM+ user guide].

### 2.1.2.1 Boussinesq Approximation

The Boussinesq approximation makes changes only to the weight term in the fluid density of the momentum equation, ignoring changes to all other density changes due to temperature gradient. The limitation of this model is that the model assumes the changes in density to be small, it also assumes that the changes to the fluid density on the weight term to vary linearly with temperature. This means that the model can only be applicable for cases when  $T \ll T_\infty$ , where  $T_\infty$  is the ambient temperature. According to the documentation within Star-CCM+,  $\frac{T}{T_\infty} \leq 20\%$  is the limit to this model.

### 2.1.2.2 Incompressible Ideal Gas

Modeling the fluid as an ideal gas makes the model more accurate, as it allows changes to the density in all the terms of the governing equation including the convective terms in the energy and momentum equations, the mass flux terms in the continuity equation and the weight term in the momentum equation. This model is suitable for *low Mach number* cases, usually around 0.3. The model assumes the following definition for density.

$$\rho = \frac{P_{\text{abs}}}{RT}$$

Where  $P_{\text{abs}}$  is the absolute pressure.  $R$  is the gas constant.  $T$  is the temperature. The justification of limiting the use of Incompressible ideal gas model to a Mach

number of 0.3 is that in this range, the differences of hydrodynamic pressure are very small compared to the background absolute pressure.

### 2.1.2.3 Compressible Ideal Gas

The ideal compressible gas model allows the fluid density to depend on the local hydrodynamic pressure in addition to the local temperature gradient, as explained in section 2.1.2.2 this becomes relevant at higher Mach numbers, since in this study only natural convection is investigated which deals with low Mach number flows below 0.3, this model does not hold much significance.

## 2.1.3 Radiation

Radiation, unlike conduction or convection does not need a medium present between two regions to participate in heat transfer, meaning that it can transfer heat even in vacuum. Radiation is often associated with energy transfer with the help of electromagnetic waves. Radiation is omnipresent at all temperature ranges. A good example for this would be the transmission of electromagnetic waves inside the microwave oven to heat food. The net rate of heat transfer by radiation from *Stefan-Boltzmann's law* can be written as,

$$q_{\text{radiation}} = \varepsilon\sigma(T_2^4 - T_1^4) \quad (2.3)$$

Where  $q_{\text{radiation}}$  is the rate of radiative heat transfer,  $\varepsilon$  translates to the emissivity of the surface that ranges between 0 and 1. An ideal black body would have an emissivity value of 1 while an ideal reflective body would have an emissivity value of 0. Pragmatically most real-world objects have an emissivity value between 0 and 1.  $\sigma$  is the *Stefan Boltzmann* constant,  $\sigma = 5.67 \times 10^{-8} \text{W}/(\text{m}^2 \cdot \text{K}^4)$

*Surface-to-surface* radiation model with non participating media i.e clean air without any smoke or other particles since it is safe to assume it is fully transparent available within Star-CCM+ was used to build the model. The thermal radiation model calculates the surface to surface interactions between pairs of patches. These patches are sets of contiguous boundary cell faces. Patches do not straddle boundaries and can be as large as an entire boundary or as small as a boundary cell face. The emissive power and radiation properties are assumed to be uniform over the surface of each patch. This patch/face proportion can be varied and is thus important to do a patch independent study. Star-CCM+ documentation recommends using a value of 5%.

## 2.2 Thermal Contact Resistance

When two surfaces 'A' and 'B' are in contact with each other as illustrated in Figure 2.1, although these surfaces appear to be in perfect contact on a macroscopic scale, upon closer inspection have micro-asperities that give rise to surface mismatch at a microscopic scale arising due to the apparent surface roughness. This mismatch at the microscopic scale gives rise to sharp interfaces between surfaces A and B as illustrated in Figure 2.1. These sharp interfaces together make the *real contact area*

while the total area that seems to be in contact to the human eye is often termed as *apparent area of contact*. It is worth noting that the real contact area makes only a small fraction of the apparent contact area even at high pressures [3]. The factors affecting the real contact area is discussed in the following sections.

When the area changes at the interface, it leads to a drop in temperature across the interface as shown in Figure 2.1, which is proportional to the value of  $R_c$ , this relation can be explained with the help of the equation 2.2

$$R_c = \frac{\Delta T}{q} \quad (2.4)$$

Combining this with equation 2.1.1

$$R_c = \frac{\Delta T}{\left(k \frac{\Delta T_c}{\Delta x}\right)} \quad (2.5)$$

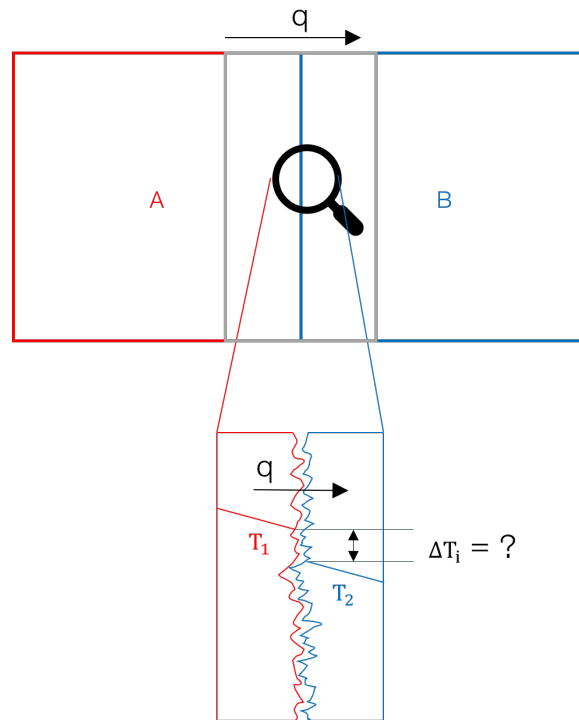


**Figure 2.1:** *Heat transfer illustration at micro scale*

It is important to note that in reality, all the three modes of heat transfer i.e., conduction, convection and radiation occur at the interface between any two surfaces in contact, however the scope of this thesis is restricted to investigating the effects of conduction, since convective and radiative heat transfer contribute very little to the overall heat transfer across the interface. The  $\Delta T$  across the interface is small and in the order of magnitude of a few Kelvin, it becomes important to include radiative heat transfer when the temperature across the interface varies more than 600 K [4].

## 2.2.1 Factors Influencing Thermal Contact Resistance

Multiple factors influence the value of  $R_c$  both directly and indirectly. These factors are listed and discussed in this subsection.

### 2.2.1.1 Thermal Conductivity

The capability of a material to conduct heat is termed as its thermal conductivity, commonly denoted by  $k$ , defined in equation 2.6. The rate of heat transfer is low with a material of low thermal conductivity and high with a material of high thermal conductivity. Thus, as the thermal conductivity of the interface between two materials in contact increases,  $R_c$  decreases. When different materials come in contact with each other, the effective thermal conductivity is calculated as described

$$k = \frac{Qd}{A\Delta T} \quad (2.6)$$

$$k_s = \frac{2k_1k_2}{k_1 + k_2} \quad (2.7)$$

### 2.2.1.2 Contact Pressure

As the contact pressure between two surfaces increases, the area of the interface along the line of contact increases [5], thus reducing  $R_c$ . This can be visualised in Figure 2.2

$$\frac{A_r}{A_n} = \frac{\frac{F}{H}}{\frac{F}{P_{avg}}} = \frac{P_{avg}}{H} \quad (2.8)$$

Where  $F$  is the load applied,  $P_{avg}$  is the average contact pressure,  $A_r$  and  $A_n$  are the real and apparent contact areas respectively and  $H$  is the Brinell Hardness.

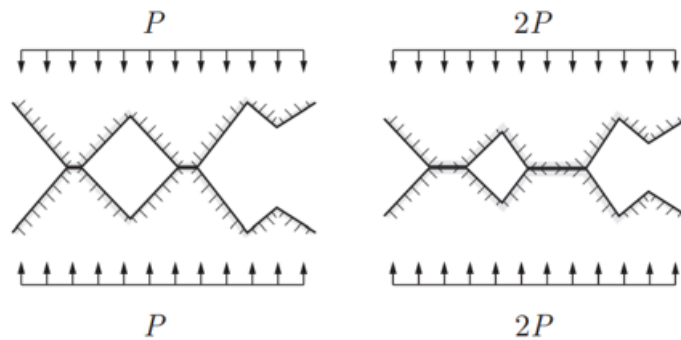


**Figure 2.2:** *Effect of increased pressure on micro asperities at the interface*

### 2.2.1.3 Surface Roughness ( $R_a$ )

Surface roughness ( $R_a$ ) is a topological survey of the material. Materials with a good surface finish have a lower surface roughness. When two surfaces with a low surface roughness come in contact, the real contact area of the interface between them is improved when compared to the same two surfaces with a lower surface finish at

the same contact pressure. This can be visualised in Figure 2.3. As the real contact area increases,  $R_c$  reduces. Thus, surface roughness and  $R_c$  are directly proportional. A commonly used representation of  $R_a$  is the RMS-roughness shortly presented in equation 2.9. RMS-roughness is the standard deviation of the distribution of the roughness height to the mean line.

$$\sigma = \text{RMS} = \sqrt{\frac{1}{l} \int_{x=0}^{x=l} |z(x)|^2 dx} \quad (2.9)$$

Where  $l$  is the length of the sample,  $z(x)$  is the height of the asperity relative to the mean line at a position say  $x$ . Assuming that the height of this surface roughness has a Gaussian distribution, the following relation holds true [refer

$$\sigma = \sqrt{\frac{\pi}{2}} R_a \approx 1.25 R_a \quad (2.10)$$

$$\sigma_s = \sqrt{\sigma_1^2 + \sigma_2^2} \quad (2.11)$$

Where  $\sigma_s$  is the effective surface roughness when different materials are in contact.

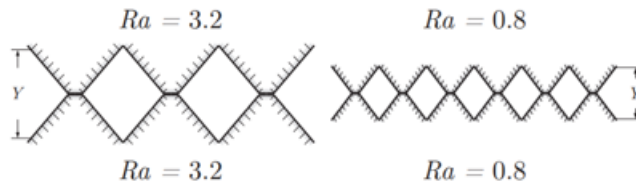


**Figure 2.3:** *Effect of decreased surface roughness on micro asperities at the interface*

#### 2.2.1.4 Asperity Slope (m)

When two materials come in contact, the real contact area is derived from the area of interfaces that meet at certain asperity points. As the name suggests, Asperity Slope (m) is the measure of the slope of the asperities at which the real contact area is formed. Thus, when the asperity slope is low the real contact area increases and thus  $R_c$  reduces. When two different materials come in contact with each other the effective asperity slope ( $m_s$ ) is described as follows,

$$m_s = \sqrt{m_1^2 + m_2^2} \quad (2.12)$$

#### 2.2.1.5 Micro-Hardness and Modulus of Elasticity

It is important to consider the deformation of the asperities as the contact pressure increases, softer materials are subject to more pronounced deformation at smaller loads and vice versa. When these asperities deform, they conform, thus increasing the real contact area. This can be better understood, visually in Figure 2.4. When the real contact area increases,  $R_c$  reduces.

Similar to the behaviour of micro-Hardness, a material with low modulus of elasticity

will deform more both elastically and plastically, thus forcing the asperities on the micro-scale to conform, resulting in a lower value of  $R_c$ .

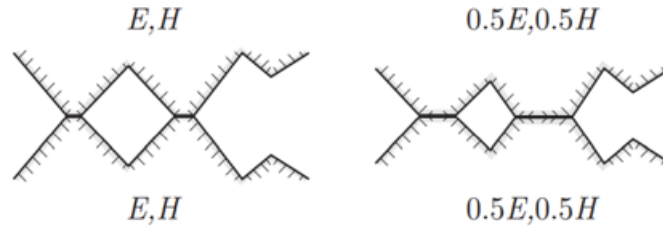


**Figure 2.4:** *Effect of decreased material hardness on micro asperities at the interface*

## 2.3 Thermal Contact Resistance Prediction

Several models have been proposed and implemented with varying success over the years to predict the value of  $R_c$ . These various models can be categorised based on the model's assumption on the nature of the micro contact deformation. Some of these models and their assumptions will be discussed in this section.

As discussed in section 2.2.1.2 while it is true that the real contact area increases with the applied contact pressure, it led some earlier researchers to believe that the deformations of the micro-asperities are purely plastic in nature. However, these assumptions are not true for most real-world scenarios [6].

While it is true that these asperities at the point of contact, behave like micro indenters on the softer material, implying that any pressure applied essentially translates to be the effect of micro hardness of the contact i.e., the stress exceeds the yield stress of the material since the area of contact is very small, causing the deformations to be purely plastic. However, at points slightly further away there exist regions of elastic deformations since the stress does not exceed the yield stress of the material at those points. This elastic deformation reduces the gap thickness and leads to the formation of more micro contacts, essentially reducing  $R_c$ . thus, it is safe to conclude that there are regions of plastic deformation surrounded by regions of elastic deformation and since they influence each other [4].

### 2.3.1 Plastic Deformation Models

This section covers the prominent contact resistance models that assume the micro-asperities to be undergoing plastic deformation.

#### 2.3.1.1 Cooper, Mikic and Yovanovich Model

In 1968, Cooper, Mikic and Yovanovich (CMY) [7] [8] proposed a model after conducting experimental study in vacuum on a set of nominally flat and rough surfaces. They assumed Gaussian distribution of surface heights and formed equation 2.13 for

the thermal Contact Conductance ( $h_c$ ).

$$h_c = 1.45 \frac{m_s k_s}{\sigma} \left( \frac{P}{H} \right)^{0.985} \quad (2.13)$$

Where,  $h_c$  is the reciprocal of  $R_c$ ,  $m_s$  is the effective asperity slope,  $k_s$  is the effective thermal conductivity,  $P$  is the contact pressure and  $H$  is the micro-hardness. Yovanovich [7], [9], later modified equation 2.13 by changing the constant to make the model more suitable to a wider range of materials.

$$h_c = 1.25 \frac{m_s k_s}{\sigma} \left( \frac{P}{H} \right)^{0.985} \quad (2.14)$$

### 2.3.1.2 Mikic Model

In 1974, Mikic [7] revisited the CMY model and further improved the correlation with experimental results. Mikic updated the relation as follows.

$$h_c = 1.13 \frac{m_s k_s}{\sigma} \left( \frac{P}{H} \right)^{0.985} \quad (2.15)$$

it is worth noting that the above presented plastic deformation models vary only with respect to the value of the constant.

## 2.3.2 Elastic Deformation Models

This section covers the prominent contact resistance models that assume the micro-asperities to be undergoing elastic deformation.

### 2.3.2.1 Greenwood and Williamson Model

In 1966, Greenwood and Williamson [5] are highly regarded for coming up with the plasticity index ( $\psi$ ), this index presented in equation 2.16 helps determine the nature of deformation of the asperities. If  $\psi \geq 1$  the deformation is almost perfectly totally plastic, if  $\psi \leq 0.6$  the deformation is almost perfectly totally elastic.

$$\psi = \left( \frac{E'}{H} \right) \sqrt{\left( \frac{\sigma}{\beta} \right)} \quad (2.16)$$

Where  $E'$  is the *effective elastic modulus* defined in equation 2.17, 'H' is the micro hardness and  $\beta$  is the radius of asperity which is assumed to be constant for all the asperities.

$$E' = \frac{E_1 E_2}{(1 - \nu_1^2) E_2 + (1 - \nu_2^2) E_1} \quad (2.17)$$

Further, the authors of the model proposed that unlike plastic deformations, during elastic deformations, the real contact area is not always linear to the contact pressure applied. They suggested that the relation between the real contact area and the pressure as follows,

$$A \propto F^{\frac{2}{3}}, \text{ Scenario 1}$$

$A \propto F$ , Scenario 2

*Scenario 1* can be described as the case during elastic deformation when an increase in contact pressure does not result in an increase in the number of micro-contact points and *Scenario 2* can be described as a case during elastic deformation when an increase in contact pressure results in an increase in the number of micro-contact points.

### 2.3.2.2 Mikic Model

In 1974, Mikic [9] revisited the Greenwood and Williamson model and updated the expression to calculate contact conductance.

$$h_c = 1.55 \frac{k_s m_s}{\sigma_s} \left( \frac{P\sqrt{2}}{E' m_s} \right) \quad (2.18)$$

Mikic developed his own criterion to check the nature of deformation of the micro asperities called the plasticity index  $\gamma$  defined as follows.

$$\gamma = \frac{H_c}{E' m_s} \quad (2.19)$$

When  $\gamma \leq 0.33$  the asperities are said to deform plastically and when  $\gamma \geq 3$  the asperities are said to deform elastically.



# 3

## Methods

In this section, the method developed to improve the thermal model of the battery is discussed. Two main goals were established to improve the thermal accuracy of the model.

The first goal was to improve the accuracy of the simulation with existing test data by explicitly modelling all modes of heat transfer even in the smallest gaps of the battery module. This is marked in red with label 5 in Figure 3.1. In reality, the electrical conducting components are covered with some layers of components for insulation purposes and the geometric differences between the two creates small air gaps. These small air gaps can vary and is roughly around 0.5 mm in height. Thus, a generic methodology was developed to efficiently model such small air gaps.

The second goal was to develop a method to estimate the Contact Resistance ( $R_c$ ) between different components in a single battery module. The contact resistance was modeled between the cells and the module cell support structure, this region is marked in pink with label 8 in Figure 3.1. The direction in which contact resistance is modeled is highlighted with an arrow marked with the same colour.

It becomes important to note that the two goals established earlier are looking at battery thermal model improvements at two different parts of the battery module. Small air gap modeling inspects the battery module in the region marked in red with label 5 in Figure 3.1 while the  $R_c$  model inspects the section marked in magenta with label 8. The main reason for concentrating on different sections was due to the larger than expected difference between the test results and the present simulation model results observed during tests that were already performed. The goals presented above aim to reduce the deviation from the physical test results.

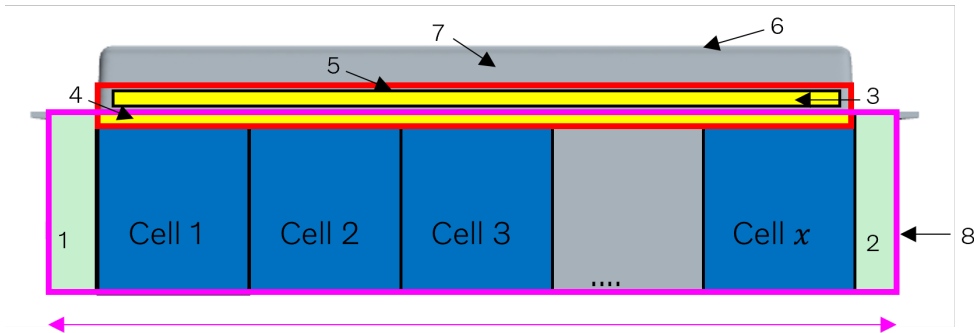


**Figure 3.1:** *Battery module schematic (not to scale)*

**Table 3.1:** *Labels for Figure 3.1*

Label	Name
1,2	Module cell support structure
3	Insulating components
4	Electrical conducting components
5	Region of interest for small air gap modeling
6	External casing
7	Air region
8	Region of interest for $R_c$ modeling

### 3.1 Small Air-gap Modeling

The thesis work began with improvements to the modeling of small air gaps present in the battery module. The motivation for modeling these small air gaps was to bring down the large difference between the test and simulation results shown in table 3.2 on two sensors with its position shown in Figure 3.3. The sensors placed in these locations from test results and probes placed in the simulation model in the same location were compared. The simulation model prior to improvements did not model the small air gaps explicitly. Only conduction heat transfer for air was modeled with the help of thermal resistivity across the boundary of the small air gap. This can be better understood with the following equation,

$$r = \frac{1}{c} = \frac{t}{k} \quad (3.1)$$

Where  $r$  is the thermal resistance,  $c$  is conductance, 't' is thickness of the material and 'k' is thermal conductivity of the medium. Modeling heat transfer in this manner accounts for only conductive heat transfer across the boundary of the small air gaps and neglects convective and radiative heat transfer. This was hypothesized to be the reason for large deviation observed between previously conducted test results and simulation predicted temperatures. The aim of this study was to first include the smallest air gaps into the computational domain by meshing it and then adding all modes of heat transfer even in the small air gaps, the results were then compared to check if there is any reduction in deviation. Different physics models of varying complexity were benchmarked against accuracy with test data and the simulation time was noted. An engineering decision was then made to choose a simulation model based on accuracy (measured as deviation between test and simulation results) and computational time.

**Table 3.2:** *Deviation observed between test data provided and baseline simulation*

Sensor Name	$\Delta T(\text{test} - \text{simulation})$ °C
Sensor 1	4.9
Sensor 2	0.5

The original model prior to this study, skipped on modeling the air volume explicitly as can be seen in Figures 3.4 and 3.5. These regions were captured into the computational domain by carrying out geometry pre-processing within Star-CCM+, using operations such as *surface wrapping* and *subtract volume*. As a reference, the smallest gap modeled with air region is 0.0004 m in height. Hence modeling such small regions required the use of custom volumetric controls for the mesher. Once the regions were well captured, a mesh sensitivity study was then carried out to study how much the mesh affected the results. Models added to the baseline model are listed in table 3.3. Some of the models listed in table 3.3 marked by the symbol '\*' are replaced with other alternative models listed in table 3.4. The interest behind trying alternate physics models was primarily to understand how close it was possible to get the computational model to the test results and also to study how adding more complex models affects the *total solver CPU time* which is a measure of how many CPU hours were required to converge the solution of the simulation. The results from this study are represented in Chapter 4.

**Table 3.3:** *Physics models and sub-models used in the improved model*

Physics Models
Gray Thermal Radiation
View Factors Calculator
Surface-to-Surface Radiation
Radiation*
Solution Interpolation
Gravity
Cell Quality Remediation
Two-Layer All y+ Wall Treatment
Wall Distance
Realizable K-Epsilon Two-Layer
K-Epsilon Turbulence*
Reynolds-Averaged Navier-Stokes*
Turbulent*
Implicit Unsteady
Segregated Fluid Temperature
Ideal Gas*
Three Dimensional
Gradients
Segregated Flow
Gas

### 3.1.1 Mesh Sensitivity

Once the air region was explicitly modeled in the battery module, a mesh sensitivity study was carried out. From table 3.5 *finer mesh* as seen in Figure A.7 was observed to yield the best results in terms of accuracy; however the computational time is roughly 4 times the *coarse mesh* as observed in Figure A.5 simulation. *fine mesh* A.6

**Table 3.4:** *Alternate Physics Models Tested*

Alternate Physics Models
Boussinesq approximation with constant density gas.
K-Omega Turbulence.
Radiation Off
Laminar flow.
Compressible and incompressible flow.

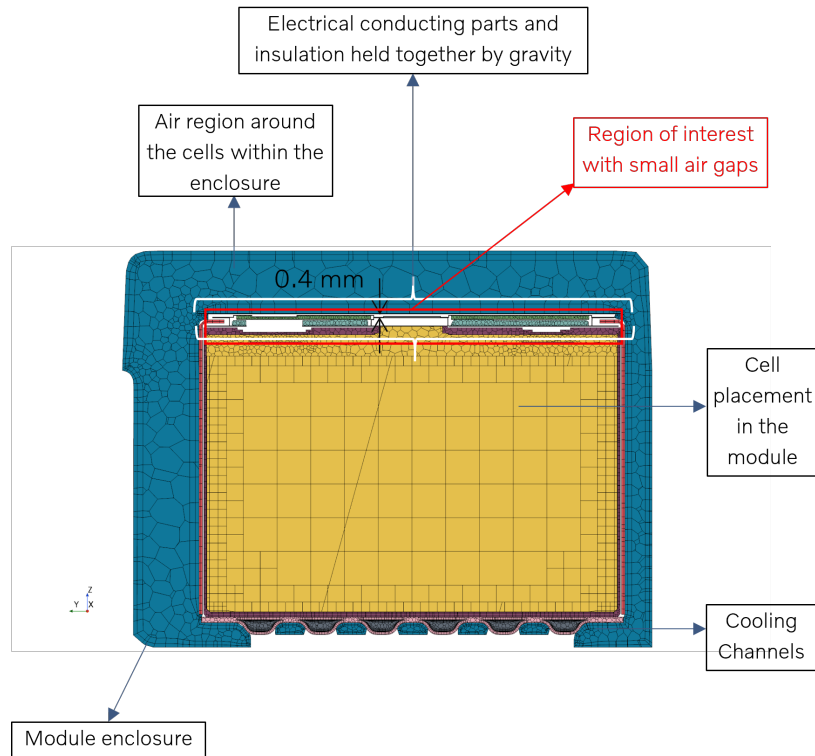


**Figure 3.2:** *Labelled cross section of the battery module*

simulation showed improvements in accuracy compared to *coarse mesh*, however, the increase in accuracy was below the permissible error from the thermocouples used in the experimental study which was  $\pm 0.3^\circ\text{C}$ . Hence, the *coarse* simulation struck the best balance between computational time and accuracy, the mesh from this simulation was chosen for all further simulations where different physics models are explored.

**Table 3.5:** *Mesh independence study*

Simulation	Comments	Mesh size ( $\times 10^6$ )	Total solver CPU time (h)	$\Delta T$ Sensor 1 $^\circ\text{C}$	$\Delta T$ Sensor 2 $^\circ\text{C}$
Base_mesh_1	Coarse mesh	5.6	393.9	2.5	0.4
Base_mesh_2	Fine mesh	13.3	805.3	2.4	0.3
Base_mesh_3	Finer mesh	23.8	1522.3	2.3	0.3

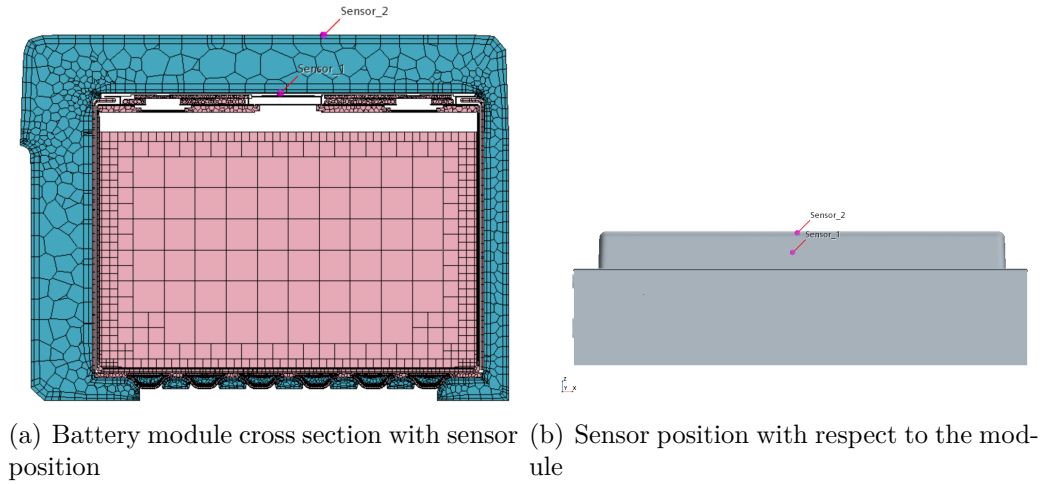


**Figure 3.3:** *Sensor positions*

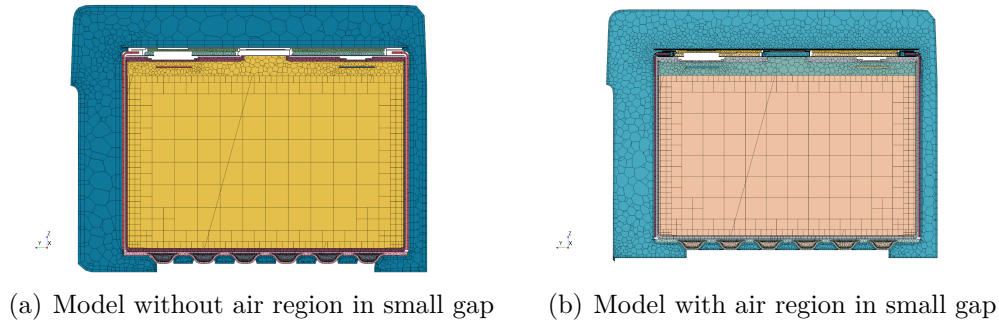


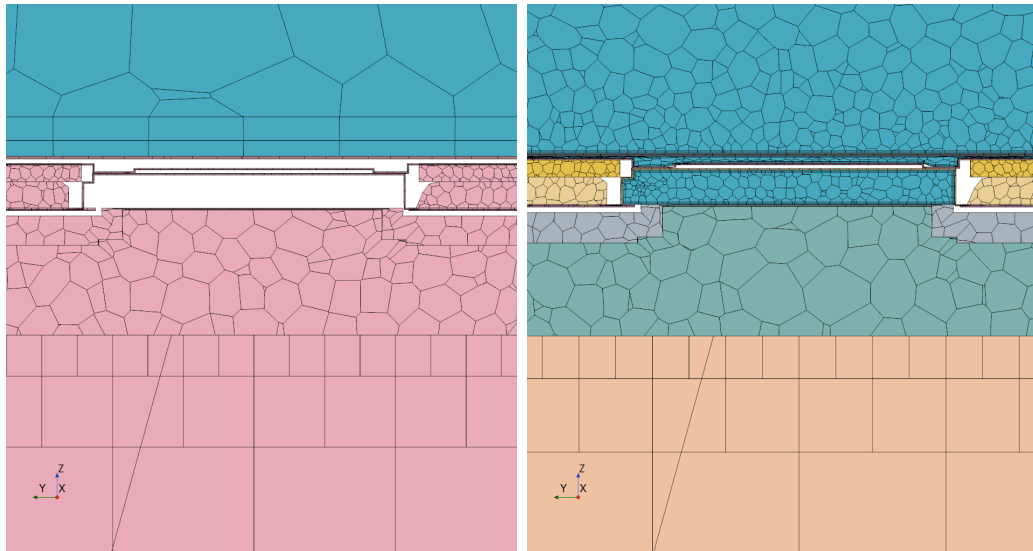
**Figure 3.4:** *Comparison of small air gap*

## 3.2 Contact Resistance Modeling

To further improve the thermal model of the battery, a methodology to model the contact resistance has been established starting with equation 2.3.2.2. The Mikic model was chosen to calculate the value of thermal contact resistance since it accounted for elastic deformation around the plastic flow of micro asperities [4]. It was also the model to best correlate with a wide range of experimental values.

It becomes important to understand the nature of deformation at the micro-contacts to efficiently model the heat transfer through it. All the interfaces under consideration, undergo elastic deformation; This was contrary to some of the previous studies that assumed only plastic deformation based on the contact pressure applied [4]. The plasticity index has been tabulated in table 3.7 along with the respective materials. Plasticity index relies on micro-hardness( $H_c$ ), effective elasticity ( $E'$ ) which in-turn relies on elastic modulus ( $E$ ) and effective asperity slope ( $m_s$ ). While efforts were made to measure material properties, certain materials in the battery pack like the thermal barrier were too soft and hence required special instruments to calculate material properties like elasticity which were not at the disposal of the thesis worker during the time of study.

From section 2.3.2.2. The following material properties were measured:



(a) Zoomed in model without air region in small gap (b) Zoomed in model with air region in small gap

**Figure 3.5:** *Zoomed in comparison of small air gap*

- Microhardness of the cell can
- Surface roughness of all the materials in use

Material properties that still exist as a range:

- Elasticity
- Thermal conductivity
- Asperity slope

Hence, literature driven values had to be used to calculate values in equations 2.15 and 2.3.2.2. These literature driven values for material properties are a range. To overcome the ambiguity, two corner cases were created, one for maximum heat transfer (HT) and the other for minimum heat transfer (HT).

### 3.2.1 Corner case 1: Maximum heat transfer

For equation 2.3.2.2, to create a case of maximum heat transfer through the micro asperities, the following combination of properties within the available range is chosen:

- $K_s$  - Maximum thermal conductivity from range
- $m_s$  - Minimum asperity slope from range
- $\sigma_s$  - Minimum surface roughness
- $P$  - Constant pressure (force/area)
- $E$  - Minimum elastic modulus

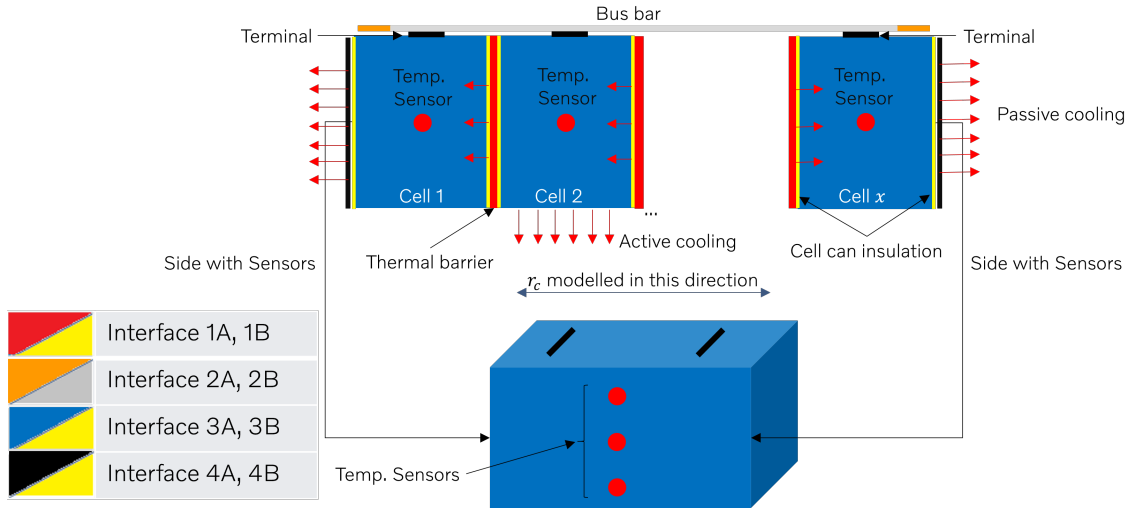


**Figure 3.6:** *Sensor and interface placement for gathered temp. data from test*

**Table 3.6:** *Interface list*

Interface	Corresponding components
1A, 1B	Thermal barrier and cell insulation
2A, 2B	Cell terminal and busbar
3A, 3B	Cell can and cell insulation
4A, 4B	Electrical isolation and cell insulation

**Table 3.7:** *Mikic Plasticity Index for corner cases ( $\gamma$ )*

Interface for Max. HT	$\gamma$	Interface for Min. HT	$\gamma$
Interface 1A	2695.61	Interface 1B	7.57
Interface 2A	59.20	Interface 2B	10.25
Interface 3A	2.34	Interface 3B	1.77
Interface 4A	31227.07	Interface 4B	80.158

From table 3.7 it is important to understand that for both the corner cases, the value of  $\gamma$  lies in the plastic deformation range as established in subsection 2.3.2.2. For interface 3A and 3B the values lie in-between the plastic range and the elastic range. However, it lies closer to the elastic deformation range ( $\gamma \geq 3$ ) than it does to the plastic deformation range ( $\gamma \leq 0.33$ ). Hence the asperities were assumed to deform elastically throughout all the interfaces and the equation 2.3.2.2 was used to calculate the thermal contact conductance through that interface.

Further, to better understand the influence or sensitivity of each interface on the overall results, the interfaces listed in table 3.7 were activated one at a time. The result from this study is presented in the section 4.



# 4

## Results

In this chapter the results from the small air gap modeling improvement and contact resistance modeling is presented. Results from the small air gap model improvement is presented first followed by the results from contact resistance study.

### 4.1 Small air gap model improvement

Results from the small air gap study described and illustrated in section 3.1 is presented here. The Several different physics models were benchmarked against *accuracy* and *total solver CPU time*. The accuracy is defined as the deviation between the physical test data and simulation results at particular probe locations. The simulation results where different physics models are utilised is presented in table 4.1.

**Table 4.1:** *Simulation bibliography*

Sl. No.	Simulation	Mesh Size ( $\times 10^6$ )	Cores	Total Solver CPU Time (h)	$\Delta T$ Sensor 1 ( $T_{Test} - T_{Sim}$ ) $^{\circ}C$	$\Delta T$ Sensor 2 ( $T_{Test} - T_{Sim}$ ) $^{\circ}C$
1	Baseline	3.4	112	155.0	4.9	0.5
2	Simulation_1	5.6	112	393.9	2.5	0.4
3	Simulation_2	5.3	112	193.1	2.4	0.4
4	Simulation_3	5.3	112	188.7	2.3	0.4
5	Simulation_4	5.3	112	232.1	2.4	0.5
6	Simulation_5	5.3	112	179.7	2.6	0.5
7	Simulation_6	5.3	112	188.3	2.4	0.3
8	Simulation_7	3.4	84	194.8	3.0	0.5

**Table 4.2:** *Simulation description*

Sl. No.	Simulation Name	Description
1	Baseline	
2	Simulation_1	Simulation includes mesh in the small air gap region. Patch/face proportion is 100%
3	Simulation_2	Same settings as "Simulation_1" with reduction in patch/face proportion from 100% to 10%
4	Simulation_3	Reduction in patch/face proportion from 100% to 5%
5	Simulation_4	5% patch to face proportion for radiation, constant density gas and Boussinesq approximation
6	Simulation_5	Simulation with no radiation modeled
7	Simulation_6	Same as "Simulation_3", turbulence model changed from realizable k-Epsilon to SST k-Omega
8	Simulation_7	Mesh in small air gap replaced by total heat transfer coefficient as boundary heat source

## Baseline simulation

Overview of physics models active in small air gap

### Models for equation of state

- Constant density with Boussinesq approximation
- Ideal gas

### Models for viscous regime

- Laminar
- Turbulent

### Models for turbulence

- K-Omega SST
- K-Epsilon Realizable

### Models for Radiation

- Grey thermal radiation

From Figure 3.5 and table 4.1, the baseline simulation has no volumetric mesh cells present in the small air gaps, instead, the heat transfer occurring through the small air gaps is simplified with a boundary heat transfer coefficient at the boundary.

## Simulation\_1

Overview of physics models active in small air gap

### Models for equation of state

- Constant density with Boussinesq approximation
- Ideal gas

### Models for viscous regime

- Laminar
- Turbulent

### Models for turbulence

- K-Omega SST
- K-Epsilon Realizable

### Models for Radiation

- Grey thermal radiation with 100% patch to face proportion

This simulation adds volumetric mesh in the small air gaps and explicitly models all modes of heat transfer. As a result of this, the accuracy between test data and simulation was greatly improved. The deviation was now reduced to 2.5 °C. The total solver CPU time of this simulation was high and increased by 154%.

## Simulation\_2

Here, all the physics models from "Base\_mesh\_1" simulation were retained and the radiation "patch to face" proportion was reduced from 100% to 10%. This significantly reduced the "total solver CPU time" from 393.9 to 193.1 hours, while improving accuracy on *sensor 1* by 0.1 °C and maintaining the same accuracy on *sensor 2*. Mesh count for this simulation drops from 5.6 million elements to 5.3 million elements as certain elements that were not participating in heat transfer on non crucial components were removed.

## Simulation\_3

Here, the radiation "patch to face" proportion was further reduced to 5%. The physics models used remain the same as in "Base\_mesh\_1" simulation. This is the recommended proportion by Star-CCM+ in its manual. Using this setting for radiation further reduced computational time while increasing accuracy on *sensor 1*. Thus, this setting of 5% "patch to face" proportion was used for all further studies.

## Simulation\_4

Overview of physics models active in small air gap

### Models for equation of state

- Constant density with Boussinesq approximation
- Ideal gas

### Models for viscous regime

- Laminar
- Turbulent

### Models for turbulence

- K-Omega SST
- K-Epsilon Realizable

### Models for Radiation

- Grey thermal radiation with 5% patch to face proportion

In this simulation, ideal gas model for equation of state was replaced by constant density gas model with Boussinesq approximations to model buoyancy effects of air due to natural convection. The Boussinesq approximation ignores any changes in the fluid density due to temperature gradients except in the weight term in the momentum equation. The fluid density appearing in the weight term is further assumed to vary linearly with respect to changes in temperature. The limitation on the appropriateness of the Boussinesq approximation is that the changes in density must be 'small'. According to the technical manual in Star-CCM+  $T/T_0$  of 10-20% is considered the limit for Boussinesq approximation, where  $T_0$  is the ambient temperature. This was checked and made sure that the model was applicable. Using the Boussinesq approximation model resulted in longer convergence time with a marginal reduction in accuracy of  $\Delta T$  from 2.3 °C to 2.4 °C. Hence, the constant

density gas model with Boussinesq approximation was ignored for the consideration and calculation of equation of state.

### **Simulation\_5**

Overview of physics models active in small air gap

#### Models for equation of state

- Constant density with Boussinesq approximation
- Ideal gas

#### Models for viscous regime

- Laminar
- Turbulent

#### Models for turbulence

- K-Omega SST
- K-Epsilon Realizable

#### Models for Radiation

- Grey thermal radiation

From table 4.1 it is evident that using the radiation model helped reduce the deviation observed between test and simulation, thus implying that radiation plays a significant role in the total heat transfer across the small air gaps; As removing the radiation physics from the simulation resulted in an increase in  $\Delta T$  on sensor 1 from 2.3 °C in "Base\_1\_5" to 2.6 °C and more importantly removing the radiation model did not result in savings in terms of simulation time.

### **Simulation\_6**

Overview of physics models active in small air gap

#### Models for equation of state

- Constant density with Boussinesq approximation
- Ideal gas

#### Models for viscous regime

- Laminar
- Turbulent

#### Models for turbulence

- K-Omega SST
- K-Epsilon Realizable

#### Models for Radiation

- Grey thermal radiation with 5% patch to face proportion

In this simulation, the k-Epsilon turbulence model was replaced with k-Omega SST turbulence model with radiation physics turned on and with a proportion of 5%

"patch to face". It was noticed that the k-Omega SST turbulence model converged marginally faster than the realizable k-Epsilon turbulence model by 0.4 hours in total solver CPU time and roughly the same accuracy as the k-Epsilon turbulence case. This simulation increased the deviation between test and simulation data on sensor 1 by 0.1°C and reduced the deviation on sensor 2 by 0.1°C.

### Simulation\_7

The total heat transfer was recorded as a report from "Simulation\_6" and plugged in as a boundary condition in "Simulation\_7". This boundary condition replaces the mesh in the small air gap region. This can be better understood with the help of Figure 4.1. Note that this simulation uses the same strategy as the "Baseline" simulation that added boundary heat flux conditions to model the heat transfer, except this simulation model captured total heat transfer coefficient which included convection and radiation. The earlier simulation only accounted for conductive heat transfer. The total CPU time for this simulation was 194.8 hours and only 84 cores were used, hence showing an improvement in time saved compared to Simulation\_6" with a drop in accuracy from 2.4°C deviation to 3°C deviation.

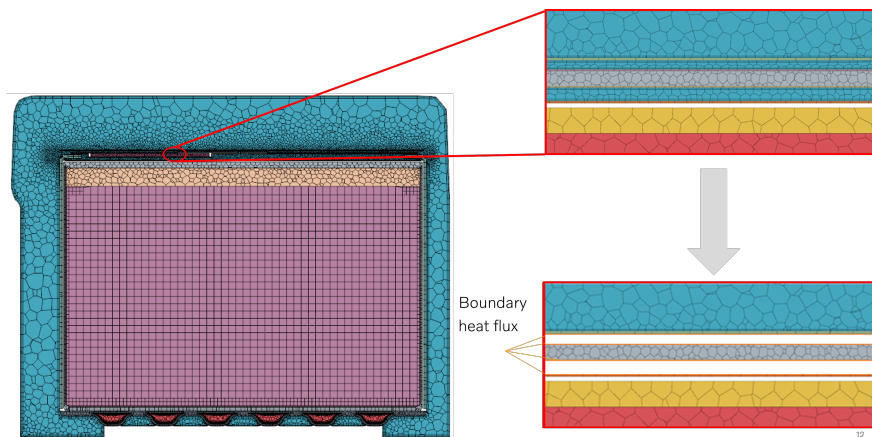


**Figure 4.1:** Schematic of mesh deletion and application of boundary heat flux

#### 4.1.1 Summary

Heat transfer in the thermal simulation model was substantially improved. Important results from Table 4.1 are represented in terms of a simple bar graph in Figure ???. This confirms that the "Baseline" model oversimplified the heat transfer within the small air gaps and explicitly modeling heat transfer in these small regions is beneficial leading to an improvement in accuracy of over 50% on sensor 1 and over 30% on sensor 2 in both simulation 3 and simulation 6. While Simulation 3 and simulation 6 yielded roughly the same level of accuracy, simulation 6 was chosen over simulation 3 due to an improvement observed in terms of computational time. Simulation 6 improved the accuracy on sensor 1 and 2 by 52% and 40% respectively, consequently leading to an increase in computational time by 21%.

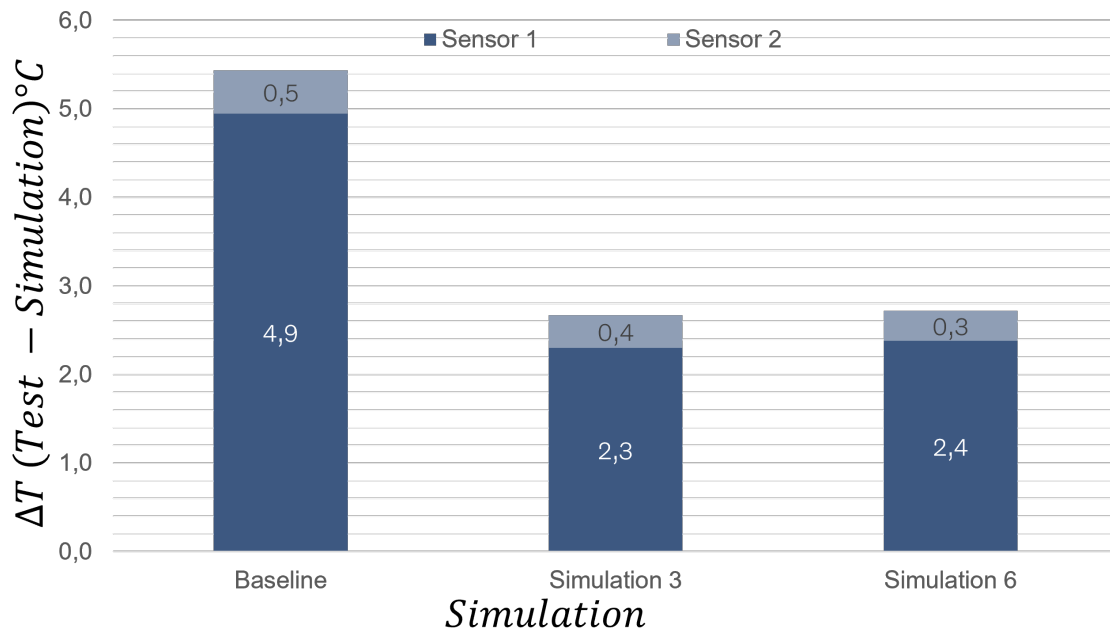


Figure 4.2: *Simulation comparison*

## 4.2 Contact resistance modeling

The results from the methodology described in section 3.2 to predict  $R_c$  will be presented in this section. Thermal contact resistance ( $R_c$ ) which is the reciprocal of thermal contact conductance ( $h_c$ ) was applied to one interface at a time and the results were saved separately and compared. The results compared are the temperature values of the simulation at probe locations that are identical to the locations at which experimental tests were carried out. Since there are multiple locations at which the sensors are placed for each cell, at each sensor location, the comparison is made. The data for cell 1 and cell 2 are presented below.

### 4.2.1 Cell 1

The sensor under consideration and its placement can be visualised with Figure 4.3

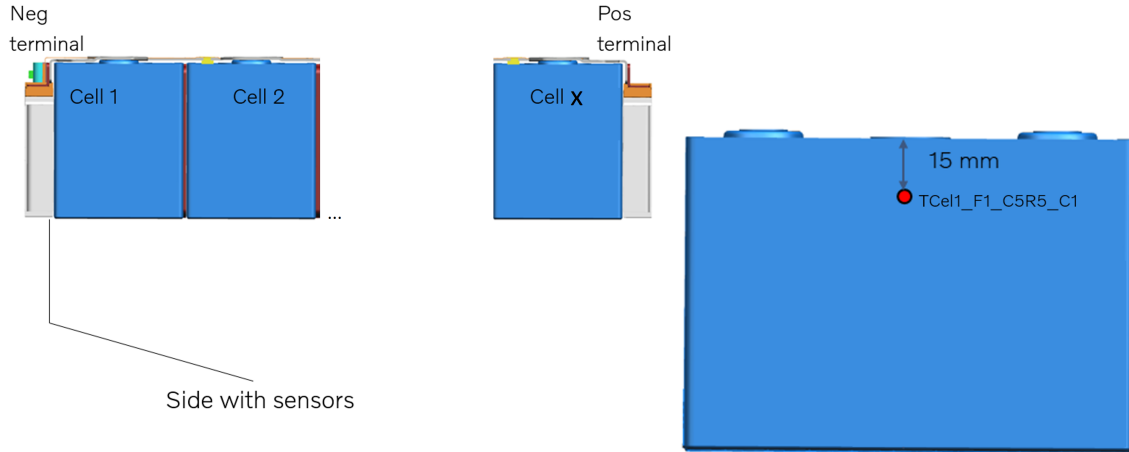


**Figure 4.3:** *Test sensor placement for cell 1*

**Table 4.3:** *Contact resistance and interface relation*

Simulation Name	$R_c$ Active on	$\Delta T$ (Test - Simulation)	Sensitivity $\Delta T$ (Baseline - current simulation)
Baseline	None	0.4162	0
001	Interface 1A	0.3914	0.0248
002	Interface 2A	0.39177	0.02443
003	Interface 3A	-0.25755	0.67375
004	Interface 4A	0.39177	0.02406
005	All interfaces active	-0.30195	0.71815
006	Interface 1B	0.39049	0.02571
007	Interface 2B	0.3945	0.0217
008	Interface 3B	-0.32161	0.73781
009	Interface 4B	0.4608	0.0446
010	All interfaces active	-0.3564	0.7726

It was observed that while modeling contact resistance largely benefited in bringing down the  $\Delta T$  between test and simulation as can be seen in Figure 4.4, it had a larger effect on interfaces 3A and 3B. This can be better understood by looking at Figure 4.5 which shows how much the current simulation has deviated from the baseline simulation which models no contact resistance on any interface. Since, contact resistance was modeled on one interface at a time, it makes sense to neglect simulations "005" and "010" in Figure 4.5 which adds contact resistances to all the interfaces present in the simulation as shown in table 4.3. It becomes important to use table 4.3 when looking at Figures 4.4 and 4.5 as doing so helps one compare the deviation between test and simulation before and after modeling contact resistance.

Considering tables 3.6, 4.3 and Figure 4.5, it is evident that modeling interfaces 3A and 3B corresponding to simulations "003" and "008" affect the results the most. Interfaces 3A and 3B are between a metal and a plastic. These interfaces are the maximum and minimum possible value of contact resistance within the range of respective material properties. For interface 3B the contact resistance value is 0.251 [ $m^2.K/W$ ] and for 3A it is 0.08 [ $m^2.K/W$ ]. In reality, contact resistance varies

between 0.08 to 0.251 [ $m^2.K/W$ ] and only the corner cases are tested here. A similar trend was observed for "cell x" and can be found in Figure A.3 and A.4.

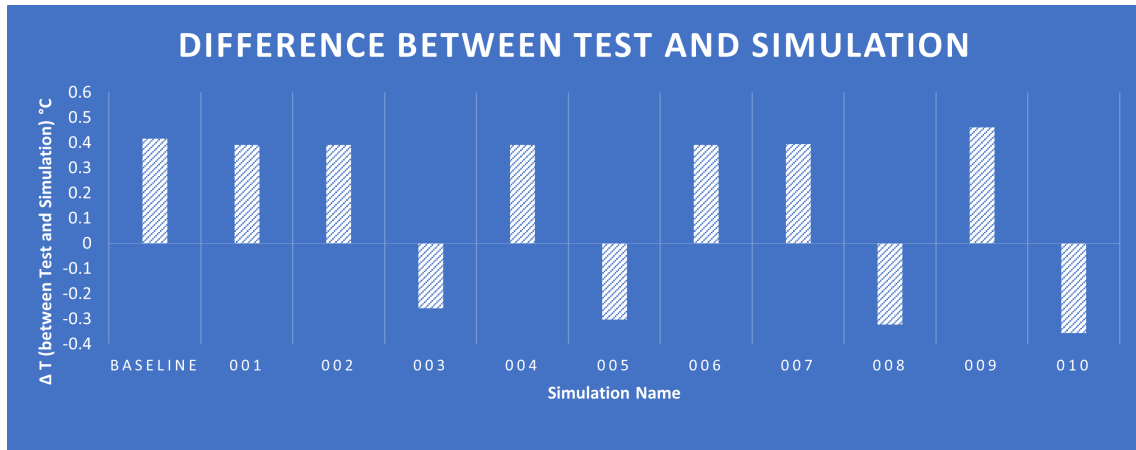


**Figure 4.4:** Deviation between test and simulation data plotted for different simulations on sensor "Tcel1\_F1\_C5R5\_C1"

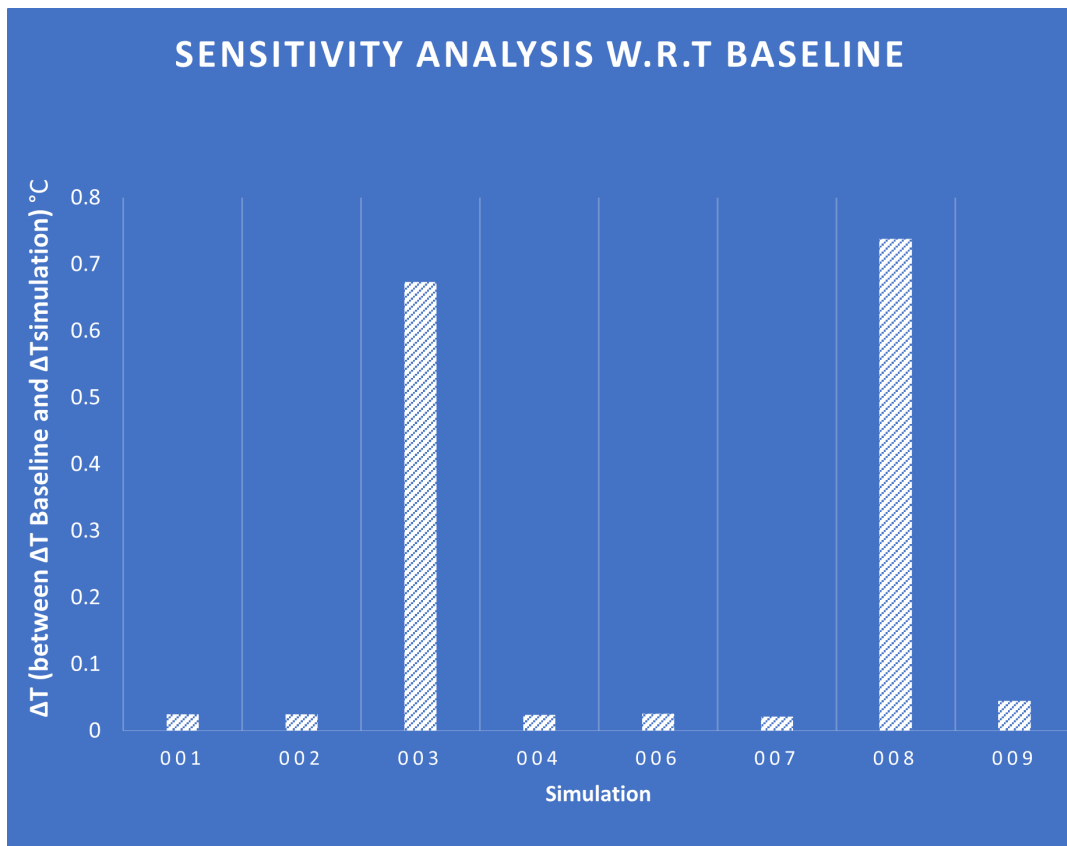


**Figure 4.5:** Deviation between current simulation and baseline simulation on sensor "Tcel1\_F1\_C5R5\_C1"

## 4.2.2 Cell 2

The sensor under consideration and its placement can be visualised with Figure 4.6

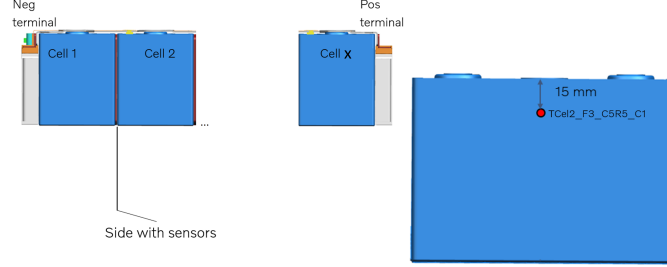


**Figure 4.6:** *Test sensor placement for cell 2*

**Table 4.4:** *Interface and simulation list*

Simulation Name	$R_c$ Active on	$\Delta T$ (Test - Simulation) $^{\circ}C$	Sensitivity $\Delta T$ (Baseline - current simulation) $^{\circ}C$
Baseline	None	0.7124	0
001	Interface 1A	0.7006	0.0118
002	Interface 2A	0.7001	0.0123
003	Interface 3A	0.6902	0.0222
004	Interface 4A	0.7021	0.0103
005	All interfaces active	0.6907	0.0217
006	Interface 1B	0.7048	0.0076
007	Interface 2B	0.7017	0.0107
008	Interface 3B	0.6897	0.0227
009	Interface 4B	0.6871	0.0253
010	All interfaces active	0.6680	0.0444

For cell 2, the same steps of comparison were carried out as in cell 1. Modeling contact resistance helped bring down the deviation between test and simulation results, as can be seen in Figure 4.7. The range of contact resistances applied remain the same here. Looking at Figure 4.8, the scale of the 'y-axis' showing the sensitivity of each simulation with respect to the baseline extends between  $5 \times 10^{-3}$  to  $3 \times 10^{-2}$   $^{\circ}C$ . This scale is much smaller than the accuracy of the thermocouples used in the test which is  $\pm 0.3$   $^{\circ}C$ . Hence, it is safe to say that it is not worth modeling contact resistance between different material interfaces for cell 2.

The reason for this is that since heat transfer only in the horizontal direction is considered and thermal contact resistance is modeled only in that direction, the effect the contact resistance will have on varying the simulation results depends primarily on the magnitude of heat transfer in the horizontal direction at that location. For cells 2 and 3 (that are placed in-between cells 1 and 4), there is very little heat flowing through the horizontal direction compared to the vertically downward direction towards the cooling plate, termed as "active cooling". For cells 1 and 4, there is a larger magnitude of heat flowing in the horizontal direction due to the presence of the endplate that behaves like a heat sink, otherwise termed as "passive cooling". This can be better understood from Figure 3.6 which shows the directions of active and passive cooling.

A similar trend can be observed for cell the last but one cell i.e. cell  $(x - 1)$  in Figures A.1 and A.2.

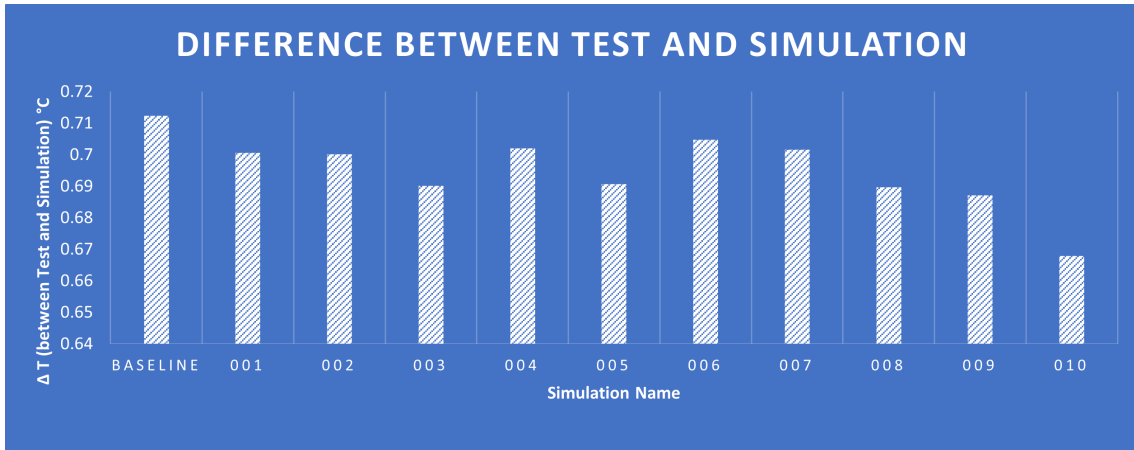


**Figure 4.7:** *Temperature deviation between test and simulation data plotted for different simulations on sensor "Tcel2\_F3\_C5R5\_C1"*

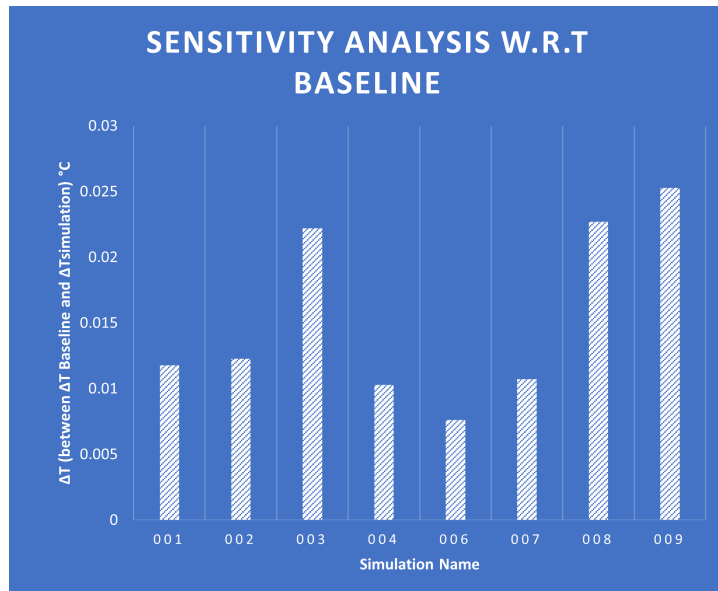


**Figure 4.8:** *Temperature deviation between current simulation and baseline simulation on sensor "Tcel2\_F3\_C5R5\_C1"*

# 5

## Conclusion

This chapter covers concluding remarks for the goals defined in this study followed by suggestions for how this thesis work could be developed further.

### 5.1 Small air gap modeling

Explicit modeling of all modes of heat transfer within small air gaps was successful in bringing down the deviation between test and simulation data, thus implying that the accuracy was improved.

- Temperature accuracy was improved by 52% on sensor 1 between physical test and simulation
- Temperature Accuracy was improved by 40% on sensor 2 between physical test and simulation
- Explicit modeling resulted in the simulation time increasing by around 20%

### 5.2 Contact resistance modeling

A methodology was clearly outlined to predict contact resistance. The material properties that influence contact resistance was discussed and the importance of the role of nature of deformation at the micro asperities in predicting the overall thermal contact resistance was highlighted. Out of all the material interface pairs considered in this study, it was found that modeling the contact resistance at the interface between a metal and soft plastic i.e., between the cell can and the cell isolation material had the largest influence on the overall simulation temperature prediction. This confirmed well with theory outlined from previous work, "Modeling thermal contact resistance becomes significant especially for interfaces where the properties of the materials that come in contact vary drastically" [4].

### 5.3 Future work

The material properties at interface 3A and 3B from table 3.6 vary drastically, as it represents a metal coming in contact with a nonmetal. Thus, it makes sense to identify such component pairs throughout the battery module and plan for experimental tests to acquire exact material properties. It is safe to state that so long as the temperature difference is not high, modeling thermal contact resistance can

be ignored on material pairs whose physical properties listed in section 3.2 does not change drastically such as aluminium to copper contact.

# Bibliography

- [1] Hans Hellsmark and Staffan Jacobsson. “Realising the potential of gasified biomass in the European Union—Policy challenges in moving from demonstration plants to a larger scale diffusion”. In: *Energy Policy*. Modeling Transport (Energy) Demand and Policies 41 (Feb. 1, 2012), pp. 507–518. ISSN: 0301-4215. DOI: 10.1016/j.enpol.2011.11.011. URL: <https://www.sciencedirect.com/science/article/pii/S0301421511008883> (visited on 06/27/2022).
- [2] *Relation between friction and adhesion*. DOI: 10.1098/rspa.1950.0097. URL: <https://royalsocietypublishing.org/doi/epdf/10.1098/rspa.1950.0097> (visited on 06/27/2022).
- [3] Victor Andersson. “Thermal Contact Conductance in Aircraft Applications”. In: *Lulea Tekniska Universitet* (2018). URL: <https://www.diva-portal.org/smash/get/diva2:1277306/FULLTEXT01.pdf>.
- [4] Karthik Narendra Babu. “THERMAL CONTACT RESISTANCE: EXPERIMENTS AND SIMULATIONS”. In: (), p. 55.
- [5] J. A. Greenwood, J. B. P. Williamson, and Frank Philip Bowden. “Contact of nominally flat surfaces”. In: *Proceedings of the Royal Society of London. Series A. Mathematical and Physical Sciences* 295.1442 (Dec. 6, 1966). Publisher: Royal Society, pp. 300–319. DOI: 10.1098/rspa.1966.0242. URL: <https://royalsocietypublishing.org/doi/10.1098/rspa.1966.0242> (visited on 06/27/2022).
- [6] *doi:10.1016/j.ijheatmasstransfer.2005.02.033 | Elsevier Enhanced Reader*. DOI: 10.1016/j.ijheatmasstransfer.2005.02.033. URL: <https://reader.elsevier.com/reader/sd/pii/S001793100500195X?token=24A088165F782918246B7C68E6D6originRegion=eu-west-1&originCreation=20220627155531> (visited on 06/27/2022).
- [7] ALBIN K J. HASSELSTRÖM U. ESKIL NILSSON. *Thermal Contact Conductance in Bolted Joints*. 2012. URL: <https://publications.lib.chalmers.se/records/fulltext/159027.pdf>.
- [8] M. G. Cooper, B. B. Mikic, and M. M. Yovanovich. “Thermal contact conductance”. In: *International Journal of Heat and Mass Transfer* 12.3 (Mar. 1, 1969), pp. 279–300. ISSN: 0017-9310. DOI: 10.1016/0017-9310(69)90011-8. URL: <https://www.sciencedirect.com/science/article/pii/0017931069900118> (visited on 06/27/2022).
- [9] B. B. Mikić. “Thermal contact conductance; theoretical considerations”. In: *International Journal of Heat and Mass Transfer* 17.2 (Feb. 1, 1974), pp. 205–214. ISSN: 0017-9310. DOI: 10.1016/0017-9310(74)90082-9. URL: <https://>

[www.sciencedirect.com/science/article/pii/0017931074900829](http://www.sciencedirect.com/science/article/pii/0017931074900829) (visited on 07/10/2022).

# A

## Extra Figures

This section of the report will contain supporting documents that supplement the information mentioned in the earlier sections.

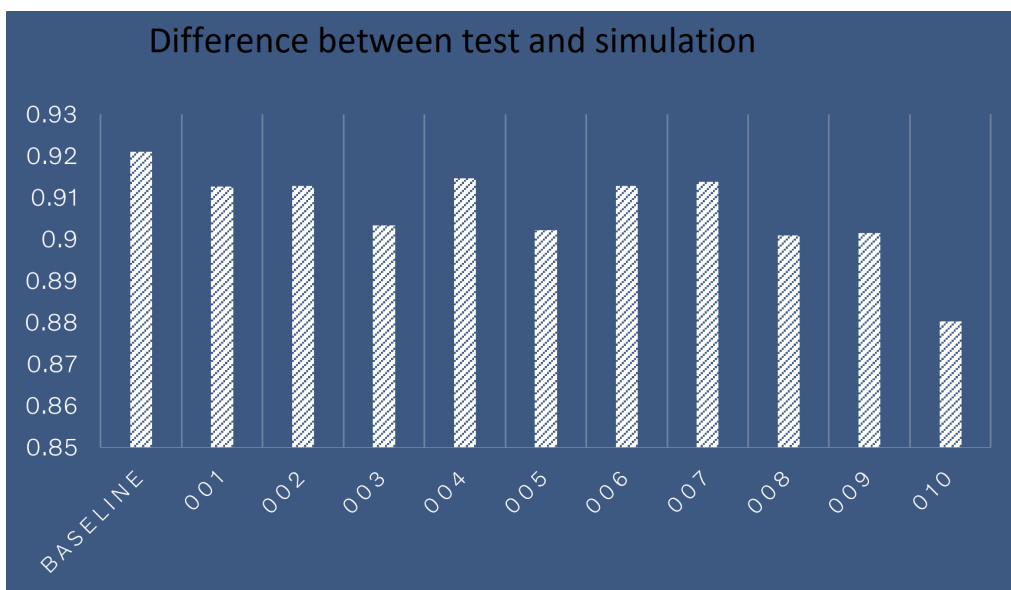


**Figure A.1:** *Temperature deviation between test and simulation on cell  $(x - 1)$*

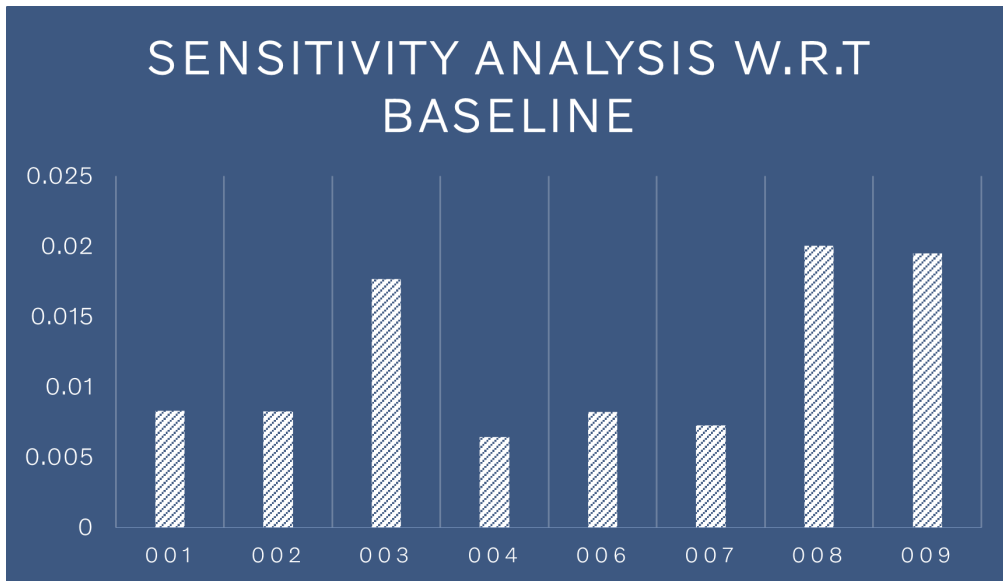


**Figure A.2:** *Temperature deviation between current simulation and baseline simulation on cell  $(x - 1)$*

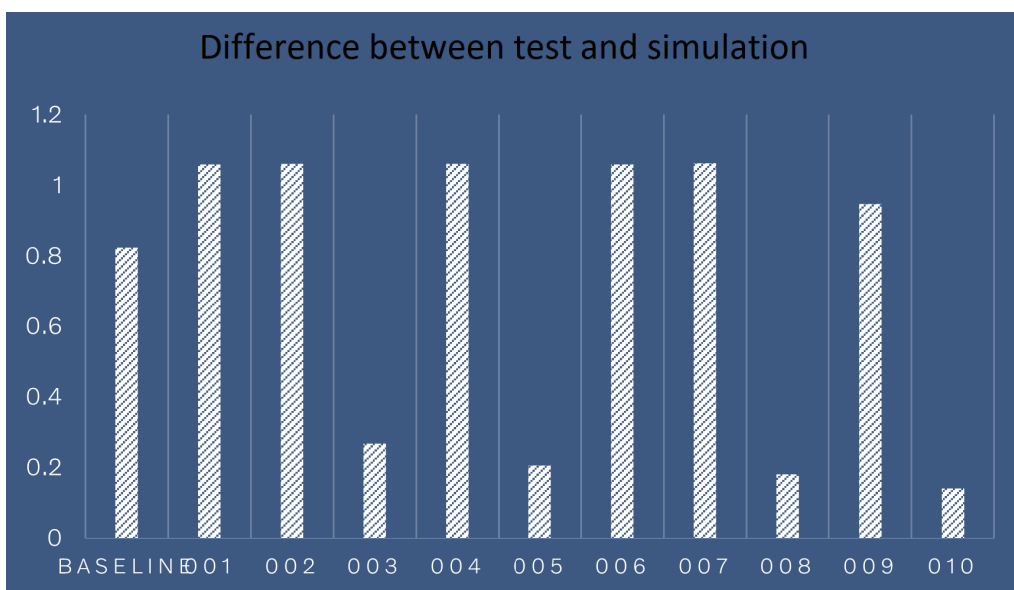


**Figure A.3:** *Temperature deviation between test and simulation data on cell  $x$*

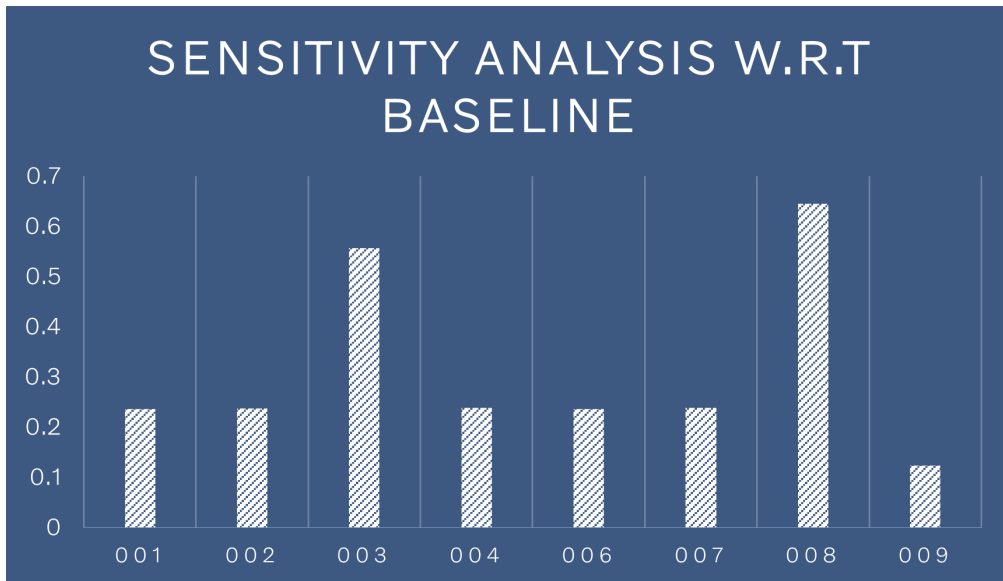


**Figure A.4:** *Temperature deviation between current simulation and baseline simulation on cell  $x$*

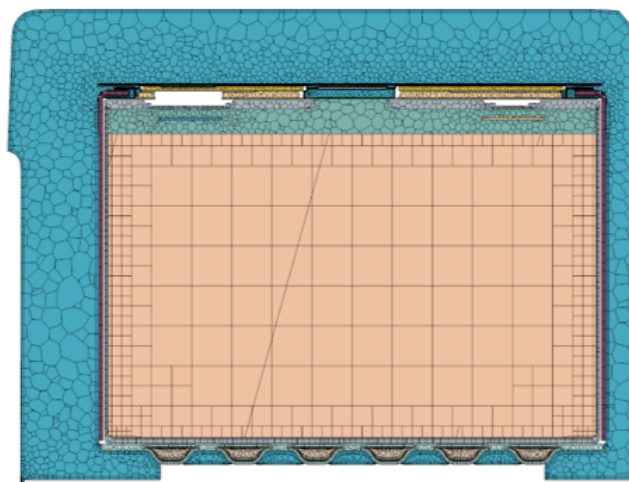


**Figure A.5:** *Coarse mesh on cross section of battery module*

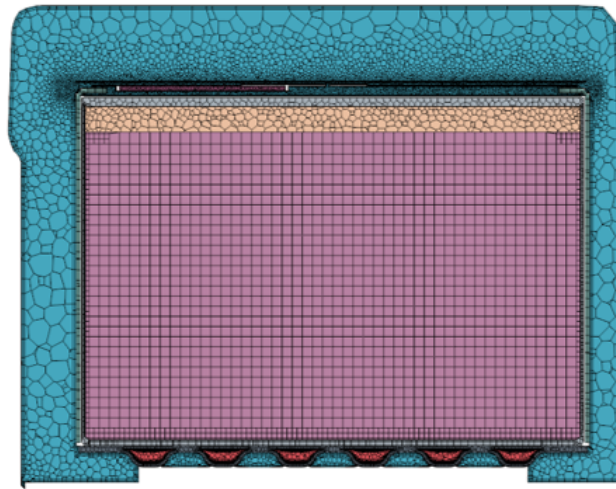


**Figure A.6:** *Fine mesh on cross section of battery module*

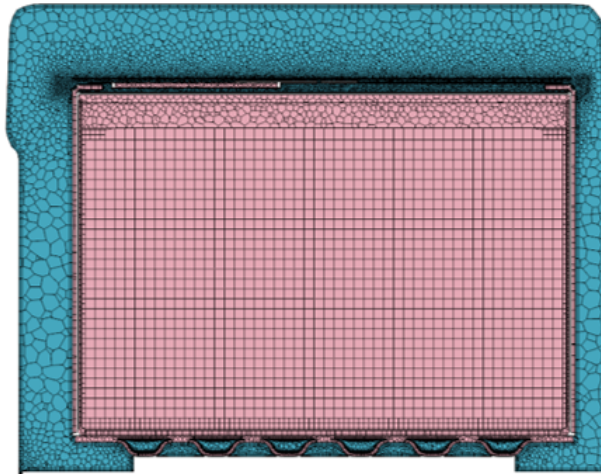


**Figure A.7:** *Finer mesh on cross section of battery module*

DEPARTMENT OF MECHANICS AND MARITIME SCIENCES  
CHALMERS UNIVERSITY OF TECHNOLOGY  
Gothenburg, Sweden  
[www.chalmers.se](http://www.chalmers.se)



**CHALMERS**  
UNIVERSITY OF TECHNOLOGY